



Two-dimensional wavefront characterization of adaptable corrective optics and Kirkpatrick–Baez mirror system using ptychography

THOMAS E. J. MOXHAM,^{1,2} VISHAL DHAMGAYE,^{2,3} 
DAVID LAUNDY,^{2,*}  OLIVER J. L. FOX,² HOSSEIN KHOSROABADI,²
KAWAL SAWHNEY,²  AND ALEXANDER M. KORSUNSKY¹

¹Department of Engineering Science, University of Oxford, Parks Road, Oxford OX1 3PJ, United Kingdom

²Diamond Light Source, Harwell Science and Innovation Campus, Didcot OX11 0DE, United Kingdom

³Synchrotron Utilization Section, Raja Ramanna Centre for Advanced Technology, Indore 452 013, India

*david.laundy@diamond.ac.uk

Abstract: Aberrations introduced during fabrication degrade the performance of X-ray optics and their ability to achieve diffraction limited focusing. Corrective optics can counteract these errors by introducing wavefront perturbations prior to the optic which cancel out the distortions. Here we demonstrate two-dimensional wavefront correction of an aberrated Kirkpatrick-Baez mirror pair using adaptable refractive structures. The resulting two-dimensional wavefront is measured using hard X-ray ptychography to recover the complex probe wavefield with high spatial resolution and model the optical performance under coherent conditions. The optical performance including the beam caustic, focal profile and wavefront error is examined before and after correction with both mirrors found to be diffraction limited after correcting. The results will be applicable to a wide variety of high numerical aperture X-ray optics aiming to achieve diffraction limited focussing using low emittance sources.

© 2022 Optica Publishing Group under the terms of the [Optica Open Access Publishing Agreement](#)

1. Introduction

Synchrotron and X-ray free electron laser (XFEL) sources produce X-ray radiation with high flux, low emittance and short pulse duration allowing dynamical systems to be studied *in situ* with high spatial and temporal resolution. Through successive generations of undulator technology the electron beam source has been compressed into ever smaller volumes of phase space and now produces diffraction limited hard X-rays in both the horizontal and vertical directions. In order to exploit these sources for nanoprobe and microprobe experiments, a large proportion of the radiation must be collected while maintaining an undistorted X-ray wavefront. After the geometric source magnification factor, fabrication errors such as mirror slope errors make the largest contribution to the focal size and are the main limiting factor for obtaining diffraction limited focusing. These errors cause undesired perturbations of the X-ray wavefront, which when propagated to the focal plane cause degradation to the focus by increasing the full width half maximum (FWHM) and decreasing the peak intensity which ends up in the focal tails.

Numerous solutions have been proposed and demonstrated to correct these errors including ion beam figuring [1], bimorph mirrors [2] and custom refractive optics [3,4]. Results obtained using specially designed refractive phase plates to compensate for the residual fabrication errors have shown particularly good improvements; however, they require precise knowledge of the error, multiple measurements and time in-between to fabricate. These types of correctors are only valid for the designed optic and may also be energy dependent. We have previously demonstrated a new type of adaptable refractive optic which is capable of dynamically correcting various

wavefront error profiles without *a priori* measurements [5]. This consists of refractive profiles with thicknesses varying in terms of their period, amplitude and phase that can be adjusted to impose any desired sinusoidal perturbation on the incident wavefront. By doing so the wavefront can be preconditioned with a profile that closely matches the reversed measured error in order to cancel out the effect of the aberrations on the focus.

Achieving such corrections requires precise knowledge of the perturbed wavefront and has led to the development of so called at-wavelength techniques [6]. These methods are performed *in situ* and at the designed wavelength of the optic, in order to measure the wavefront error of optics as they would be used as well as quantify the effect of corrective optics. Common at-wavelength techniques such as speckle tracking [7], Hartmann sensing [8], grating interferometry [9] and pencil-beam scanning [10] are ray based techniques and ultimately limited by the fabrication accuracy of the deflecting structures and detector pixel size. Ptychography overcomes these resolution limitations by using multiple diffraction patterns acquired by scanning a test sample to recover the complex probe and transmission functions [11,12]. It has been used extensively to characterize nano-focusing optics [13–17] and to measure wavefront errors [18], as the recovered complex wavefield of the probe can be propagated to any plane along the optical axis. Although a highly coherent probe is normally required, customized algorithms [19,20] and post processing procedures [21] can account for decoherence effects. Its use as a metrology technique for X-ray optics with partial coherence has been previously demonstrated by the present [20,22] and other [23,24] authors. We report making use of our prior results later in the article.

Here we further investigate the effect of adaptable refractive correctors on the wavefront error and focusing performance of a Kirkpatrick–Baez mirror system. Compared with our previous work which only considered correction in one-dimension, in the present work we successfully correct the horizontal and vertical focusing mirrors simultaneously. We employ a ptychographic metrology technique which is able to reconstruct the two-dimensional probe without the effect of a geometric source factor i.e., for the fully coherent case. This is beneficial over other conventional metrology techniques which normally measure the wavefront error and then superimpose it on an ideal optic profile to assess the effect on focusing performance under coherent conditions. The horizontal and vertical wavefront error components are also shown to decompose orthogonally to one another and the corrected focus is found to be diffraction limited. The recovered probe is additionally used to simulate the benefits of corrective optics on a typical scanning transmission X-ray microscopy experiment of Au nanoparticles. As the vertical focusing mirror employed for the experiment is already of comparatively low figure error a discussion follows of the situations which necessitate wavefront error correction and the associated benefits and drawbacks.

2. Adaptable wavefront correction

To achieve nanometre diffraction limited focal spot sizes, optics with high efficiency and large numerical aperture (NA) must focus light with minimal wavefront distortion. This places huge demands on fabrication methods and good quality X-ray mirrors can cost hundreds of thousands of pounds to produce and require many months to years of waiting for production to complete. Mirror quality is primarily determined by its figure error, that is the deviation of the surface from an ideal ellipse. The resulting wavefront error $w(x, y)$ is related to the figure error $\Delta h(x, y)$ and grazing angle of incidence α by [25],

$$w(x, y) = 2\Delta h(x, y) \sin(\alpha) \quad (1)$$

For hard X-rays α is typically on the order of mrad meaning that figure errors on the order of nanometers are required to give diffraction limited focusing. Graded multilayer coatings for mirrors [26] have successfully increased the NA of reflective optics by increasing the grazing angle of incidence by an order of magnitude. According to Eq. (1) these will be much more sensitive to figure errors, meaning some form of correction will be required.

Perfect optics achieve focussing by imparting a convergent spherical surface on the incident wavefield such that each part arrives in phase and interferes constructively at the focus. Deviations from this surface are defined as the wavefront error [27] and correspond to a change in path length in the direction of propagation. The wavefront error $w(x, y)$ is typically well characterized by its root mean squared (rms) value which is given by,

$$\sigma_{\text{rms}} = \sqrt{\int_{x_1}^{x_2} \int_{y_1}^{y_2} \frac{w^2(x, y)}{(x_2 - x_1)(y_2 - y_1)} dx dy} \quad (2)$$

where we have also assumed without loss of generality that the wavefront error $w(x, y)$ has zero mean defined over the length of its aperture. For small wavefront errors with $\sigma_{\text{rms}} \ll \lambda$ the central focal peak intensity is purely determined by the rms value through the Strehl ratio [27].

Many two-dimensional X-ray focusing optics consist of independent horizontal and vertical elements which are simpler to produce. This generally results in more significant fabrication errors along the direction of the focusing such that the wavefront error can be decomposed into separate one-dimensional contributions from each of the transverse elements,

$$w(x, y) = w_v(y) + w_h(x) \quad (3)$$

With mirrors for example, the grazing angle of incidence results in an illumination highly extended along the Kirkpatrick–Baez mirror's length. Whereas only a small portion is apertured across it resulting in a more significant figure error along the mirror length. This assumption means the horizontal and vertical optics can be corrected independently to one another.

The aim of wavefront correction is to introduce perturbations to the wavefront which cancel out those originating from the aberrated optic. This is well known in visible optics but has only been demonstrated recently with X-rays due to advances in microfabrication techniques such as deep X-Ray lithography [28]. The change in X-ray path-length on passing through a homogenous material with thickness profile $t(x)$ is given by,

$$\Delta X = \delta(E)t(x) \quad (4)$$

where $\delta(E)$ is the energy dependent refractive index decrement. As the refractive index decrement for most polymers is on the order $\delta(E) \sim 10^{-6}$ at hard X-ray energies, this means thicknesses of a few microns can induce path length variations on the picometer scale. Since only a small amount of material is required, absorption is negligible unlike for most X-ray refractive optics.

Our initial developments of refractive correctors focused on designing bespoke correctors for each optic [3], which involved measuring the wavefront error, designing and fabricating structures before finally installing them and confirming an error reduction. This procedure is time consuming and prone to measurement errors, thus recent developments focus on adaptable refractive correctors [5], which consist of a single set of generic correctors. These aim to correct the majority of the wavefront error by introducing a dynamical sinusoidal profile with variable period and amplitude that closely matches the reversed measured profile. The refractive structures were fabricated at Indus-2 [29] using deep X-ray lithography and a known SU-8 polymer with a high refraction to absorption ratio. The process produces high aspect ratio planar structures on a silicon substrate, the lateral depth of which can be up to 1 mm with transverse resolutions less than 1 μm . To assist with alignment fiducial markers are also included at the ends and regular intervals along the length. The adaptable correctors have previously been reported in [5].

3. Experimental setup

Experiments were performed at the B16 Test beamline at Diamond Light Source [30], a bending magnet beamline that provided an unfocused monochromatic X-ray beam. An X-ray energy

of 12 keV was selected by a double crystal monochromator with an approximate $\Delta E/E \sim 10^{-4}$ energy bandpass to maximize longitudinal coherence. In order to maximize the available flux, no source slits were used to spatially filter the transverse coherence as in normal ptychography experiments, this provided an approximate flux of 10^8 photons/s at the focal position. The beam was focused using an aberrated Kirkpatrick–Baez mirror system, which featured a vertically focusing (VKB) and horizontal focusing (HKB) set of Pd coated elliptical mirrors designed to work at 3 mrad grazing incident angle. Both mirrors have a $270\text{ }\mu\text{m}$ aperture and 125 mm horizontal and 235 mm vertical focal length respectively. These values were originally chosen to compensate the source size asymmetry of the B16 beamline, so that the focal size would be similar in both directions. Two sets of adaptable correctors, one for each mirror were positioned upstream of the mirror system perpendicular to one another and slits were used to select an incident beam size matching the mirror aperture. An experimental schematic of the setup is shown in Fig. 1.

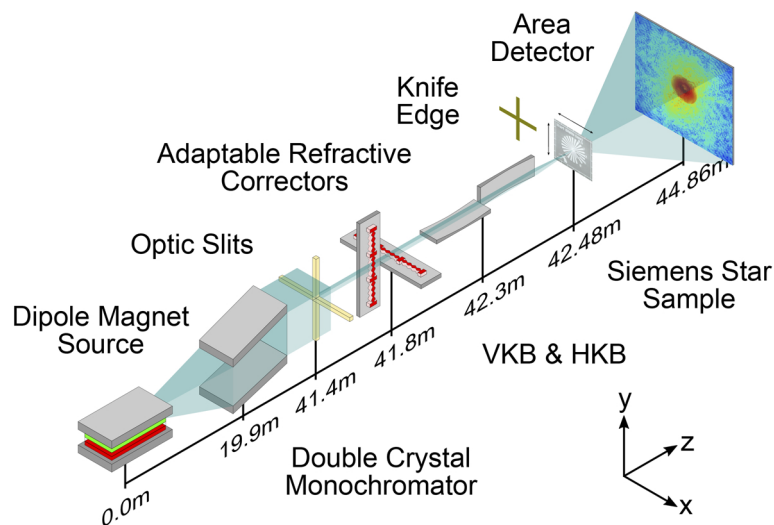


Fig. 1. Schematic of the experimental setup and distances (not to scale) used for adaptable optics correction and ptychography wavefront measurements on the B16 Test beamline at the Diamond Light Source. The X-ray beam was generated using a bending dipole magnet source, and the energy was selected using a double-crystal monochromator. The beam was then focused by a Kirkpatrick–Baez mirror system and the object scanned transversely to the beam close to the focus. Diffraction patterns were collected downstream using a single-photon counting detector.

The mirror and structure alignment was performed using a knife edge scanning method to measure the one-dimensional wavefront and is described in more detail in [5]. This uses a Au knife edge positioned close to the focal plane and is scanned in the horizontal and vertical directions as the transmitted intensity is recorded by an area detector at some known distance downstream. This allows the wavefront at each pixel of the detector to be projected back along the propagation direction to the focal plane and then back further to a plane perpendicular to the optical axis at the optical element. It is a relatively quick method of wavefront measurement but only provides the one-dimensional error. For elliptical mirrors the wavefront error includes an additional cubic component when the pitch angle is misaligned [31]. This increases linearly with angular misalignment and can therefore be optimized with only a few knife edge scans at different pitch angles and performing a linear regression.

The measured wavefront error was then analyzed to select the most appropriate period and the refractive correctors were moved to this position. The correctors were mounted on high-precision Attocube piezoelectric stages which allowed all three rotational and transverse translational degrees of freedom. Fiducial markers at the ends of the structures were used with direct beam and an area detector to align them parallel with the incident beam, similarly to how planar X-ray lenses are aligned. Each adaptable refractive corrector consists of two sinusoidal profiled structures with a slowly varying period from $40\text{ }\mu\text{m}$ to $360\text{ }\mu\text{m}$ and an amplitude of $40\text{ }\mu\text{m}$. This allows for a large range of wavefront error periods as well as a variable correction amplitude between 0 pm and 72 pm at 12 keV . The correction period and amplitude were adjusted by translation and pitch rotation of the structure respectively. The optimization procedure for the wavefront correction was as follows [5]. The measured wavefront error was used to determine the optimum period for the correction. Using this period of correction and with a small correction amplitude, the correction phase was adjusted to minimize the measured rms wavefront error. Then with the phase of the correction fixed, the amplitude of the correction was adjusted to again minimize the rms wavefront error. This process was then repeated to give the optimum wavefront correction. After the alignment of the correctors, it was found that the mirror pitch angle and the longitudinal focal position had also changed slightly and required readjusting. This is discussed more in the results section.

4. Ptychography wavefront measurements

For two-dimensional wavefront characterization ptychography was performed as it provides higher resolution than other methods [24] and can recover the coherent complex probe function. This is a coherent scanning diffraction imaging technique that uses overlapping sample diffraction patterns to solve the phase problem. More information on its implementation can be found in [11,12]. For the present measurements, a $3\text{ }\mu\text{m}$ thick Au Siemens's star on a silicon nitride substrate was positioned slightly downstream of the focal plane on high-precision Attocube piezoelectric translational stages. The Siemens star had a diameter of $400\text{ }\mu\text{m}$ and featured an inner spoke separation of $1\text{ }\mu\text{m}$ as the smallest feature size. Ptychography scans were performed by translating the sample through the beam and acquiring diffraction patterns at each position, which was done in a spiral manner to reduce raster artifacts [11]. A single-photon counting, third-generation Merlin Medipix detector with a pixel size of $55\text{ }\mu\text{m} \times 55\text{ }\mu\text{m}$ and a pixel array of $512\text{ px} \times 512\text{ px}$ was positioned 2.38 m downstream of the object.

Ptychography scans were performed over an area of $24\text{ }\mu\text{m} \times 24\text{ }\mu\text{m}$ with a 400 nm step between adjacent positions and 0.5 s exposure time which generated 7198 diffraction patterns. The probe size was also optimized to the experimental geometry [32,33] by performing a series of smaller area scans along the beam path. The scan is highly oversampled relative to similar experiments to account for the low coherent flux from the dipole source [20]. Scans were repeated with and without the refractive correctors inserted and included a slight adjustment of the individual mirror pitch angles as mentioned previously. Initial reconstructions were processed during the experimental session using the *ptypy* framework [34] and the difference map (DM) [35] reconstruction algorithm with a multi-modal probe [36]. This was performed on a reduced dataset and found to be most effective at finding an initial probe solution given only a simulated defocused ideal optic and an approximated power distribution. Post experimental reconstructions were best achieved using a multi-modal implementation of the regularized ptychographic iterative engine (rPIE) [37].

Diffraction patterns were cropped to a region of interest around the optical axis measuring $180\text{ px} \times 180\text{ px}$, which included only statistically relevant counts and resulted in a 25 nm effective pixel size. Dead and hot detector pixels were also disregarded from the reconstruction by generating a detector mask based on the integrated diffraction data stack. To recover a single coherent probe, we followed the procedure outlined in [20], where a multi-modal sample is

considered as the source of experimental decoherence. This was performed on a subset of the diffraction dataset to reduce the computational time. More details on the ptychography procedure, the reconstructed probe and object and their modal decomposition is provided in the [Supplement 1](#). Sample modes were included until the relative modal power in the final mode was negligible, which occurred at 75 modes. Reconstructions started with a flat sample function and the previously reconstructed DM probe; sample modes were then included as random permutations of the initial function. The rPIE algorithm was then run for 500 iterations until the Fourier error converged to suitable minima. The power of the coherent probe and the dominant multi-modal probe mode were found to be approximately the same. The coherent power was found to be 5.3×10^6 photons/s for the uncorrected mirror and 1.5×10^6 photons/s for the corrected mirror. The power reduction after correction occurs because of absorption within the support sections of the adaptable refractive structures, the thickness of which will be greatly reduced in future iterations due to better deep X-ray lithography fabrication methods.

Since the ptychographic technique recovers a complex scalar field, we can numerically propagate using the Fresnel-Kirchhoff equation to any plane along the optical axis in order to analyze the focal properties and beam evolution. Before further processing the power of the probes with and without correctors was equalized to account for source intensity fluctuations and absorption of the structure supports. A small cubic component corresponding to a mirror pitch misalignment that could not be optimized physically due to limitations using the knife edge technique was also fitted and subtracted, an explanation of this is provided in the [Supplement 1](#). Probes with and without the refractive correctors were propagated along the optical axis and beam caustics were generated by integrating the intensity volume along the horizontal and vertical directions. The results for this are shown in Fig. 2 which also labels the defocused position slightly downstream of the focus where ptychography scans were performed, as well as the focal planes defined as the plane which maximized peak intensity. It can be clearly seen there is a significant astigmatism between the two foci both before and after correction which could be corrected for by translating the mirrors relative to one another.

The beam caustic and focal intensity distribution only provide partial insight into the performance of an optic. To characterize completely the optical aberrations causing focal degradation and to measure the effect of corrective optics, the wavefront error at the optic plane must be calculated. We back propagated the probe wavefield upstream to each individual mirror with and without the correctors and unwrapped the phase. At each mirror position the parabolic phase $\Delta\varphi(x, y)$ of an ideal mirror was fitted and subtracted according to,

$$\Delta\varphi(x, y) = -k \left(\frac{x^2}{2f_x} + \frac{y^2}{2f_y} \right) \quad (5)$$

where k is the wave number and f_x and f_y are the effective horizontal and vertical focal lengths at that mirror position. The resulting phase error is easily converted to a path length (or wavefront) error and can be decomposed separately in horizontal and vertical contributions according to Eq. (3) by subtracting the mean error along the opposite axis. The full analysis generated four wavefront errors corresponding to the corrected and uncorrected HKB and the corrected and uncorrected VKB mirrors. These are displayed in Fig. 3(a)–3(d).

From the two-dimensional wavefront errors we can visually note a reduction in the error when refractive correctors are used. This is most apparent for the HKB mirror which features more prominent aberrations. The observation that the errors can be decomposed into their orthogonal components before correction also confirms the fact that aberrations are most apparent along the length of the mirrors. To compare with results using the one-dimensional knife edge scanning technique, the two-dimensional wavefront errors were averaged along their respective planes. The profiles in Fig. 3(e) and Fig. 3(f) and their corresponding rms values agree with the same measurements previously reported using the knife edge technique [5]. The HKB rms was reduced

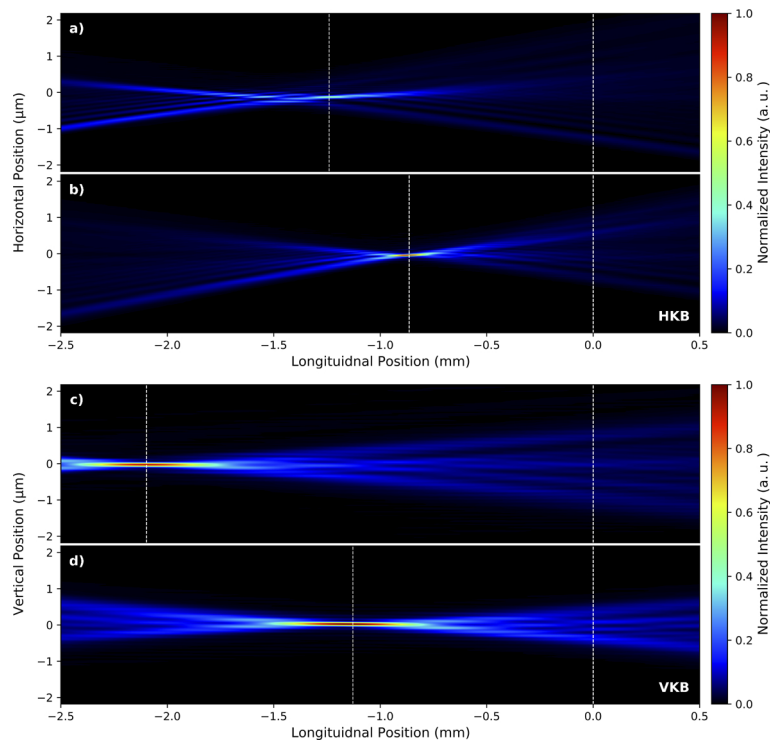


Fig. 2. Propagation of the reconstructed coherent probe using the Fresnel-Kirchhoff equation. The horizontal beam caustic, integrated along the vertical plane a) before and b) after correction. The vertical beam caustic, integrated along the horizontal plane c) before and d) after correction. The 0.0 mm line corresponds to the reconstructed probe plane and other line corresponds to the focal position in that plane.

from 17.8 pm to 4.5 pm and the VKB rms was reduced from 3.1 pm to 1.7 pm with the use of the refractive correctors. The reconstructed pixel size of 25 nm was found to clearly resolve the focal intensity with at least 3 points on the central peak and gave values closely matching the diffraction limit, therefore the probe resolution is maximized and around 50 nm. Given the same sampling period is maintained doing the propagation to the optic plane and wavefront processing, the resolution of the wavefronts is expected to be the same. The high spatial resolution of the ptychography technique is not only able to recover the larger slope error but also appears sensitive enough to measure higher frequency errors as well. This observation is important and would benefit from a dedicated study, ideally using a high quality optic that featured little to no residual slope error, and comparison with another surface analysis technique, such as atomic force microscopy or Fizeau interferometry.

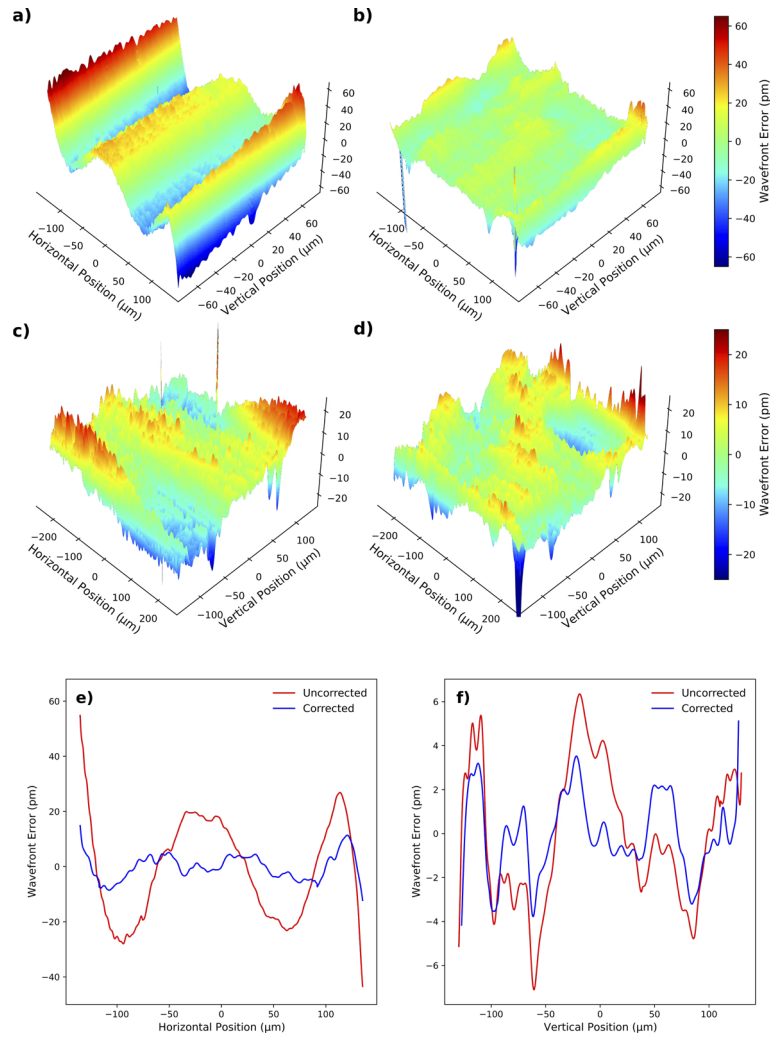


Fig. 3. Residual wavefront errors at the mirror position. The two-dimensional HKB wavefront error before a) and after b) correction. The two-dimensional VKB wavefront error before c) and d) after correction. The mean one-dimensional wavefront errors along respective planes for e) the HKB mirror and f) the VKB mirror.

5. Focal profile results

The main aim of reducing the rms wavefront error using corrective optics is to obtain a diffraction limited focal spot size and increase the central peak intensity. The size and shape of wavefront errors greatly influences the focal properties and has been extensively studied and applied most notably with their decomposition into Zernike [27] and Legendre polynomials [38]. However, for small rms wavefront errors $\sigma_{\text{rms}} \ll \lambda$ the complex wavefield exponent can be expanded into a series and results in the Strehl ratio given by [27],

$$\frac{I}{I_0} = 1 - \frac{4\pi^2\sigma_{\text{rms}}^2}{\lambda^2} \quad (6)$$

where I_0 is the ideal (zero wavefront error) peak intensity value and I is the actual (with wavefront error) peak intensity. Thus when the wavefront error is small, the focus profile is a sharp diffraction limited peak with a normalized intensity given by Eq. (6). The lost intensity then forms satellite peaks and a much broader background outside this central peak which degrades signal-to-noise for scanning probe experiments. Since diffraction limited focusing is typically defined for Strehl ratios greater than 0.8, this is realized for $\sigma_{\text{rms}} \lesssim \lambda/14$ or the Maréchal criterion.

In order to evaluate the focal properties we first added a small parabolic term along the vertical direction to correct the astigmatism both with and without the correctors. The beam caustics after the astigmatic correction are included in the [Supplement 1](#). These were then back propagated to the focal planes, defined as the plane that maximized peak intensity. This is shown in Fig. 4(a) and Fig. 4(b). At these longitudinal positions horizontal and vertical line profiles were taken at the peak intensity position and in order to evaluate the performance of each mirror separately the power of the profiles was equalized. Gaussians were fitted and found the FWHM focal size to be 60.4 nm (h) \times 77.9 nm (v) before correction and 41.1 nm (h) \times 79.5 nm (v) after correction. To compare with the ideal case we simulated the HKB and VKB mirrors using an ideal thin lens with the same aperture, focal length and incident beam flux. This gave a diffraction limited focal size of 41.7 nm (h) \times 78.5 nm (v) and agrees well with the theoretical value as well as those recovered from the measured results after correction. The Strehl ratio improved from 0.43 to 0.94 for the HKB mirror and 0.98 to 0.99 for the VKB mirror. These agree with the Strehl ratios from Eq. (6) using the wavefront error rms values found previously and mean both optics can be considered diffraction limited. The one-dimensional focal profile results are displayed in Fig. 4(c) and Fig. 4(d). The HKB correction provides the majority of peak intensity gain and horizontal focal size reduction, while the VKB sees only a very slight increase in peak intensity as it can be considered diffraction limited prior to correction.

The satellite intensity peaks and higher background noise ultimately degrade the full field and scanning transmission microscopy techniques that use focusing optics, such as fluorescence imaging. Unfortunately the large source size on the B16 Test beamline dominates the focal size contribution and makes a comparative sample study with and without the corrective structures very difficult. Instead we have simulated a typical scanning transmission X-ray microscope of nanoparticles using the coherent beam reconstructed from ptychography. A similar simulation to that presented is included in the [Supplement 1](#) using the partially coherent multi-modal probe. The simulated sample consists of randomly oriented Au nanocubes around 250 nm in size deposited on a silicon nitride substrate and positioned at the focus. The simulated imaging experiment is then simply a convolution of the sample transmission with the point spread function or focal intensity of the optical setup. The results of this are shown in Fig. 5 for the original sample, ideal, uncorrected and corrected probes and demonstrate visually the benefit of using corrective optics with little difference between the ideal and corrected images. A line profile take across the image shown in Fig. 5(e) also clearly shows the contrast improvement of the corrected optics over the uncorrected. The corrected optics don't dramatically increase the spatial

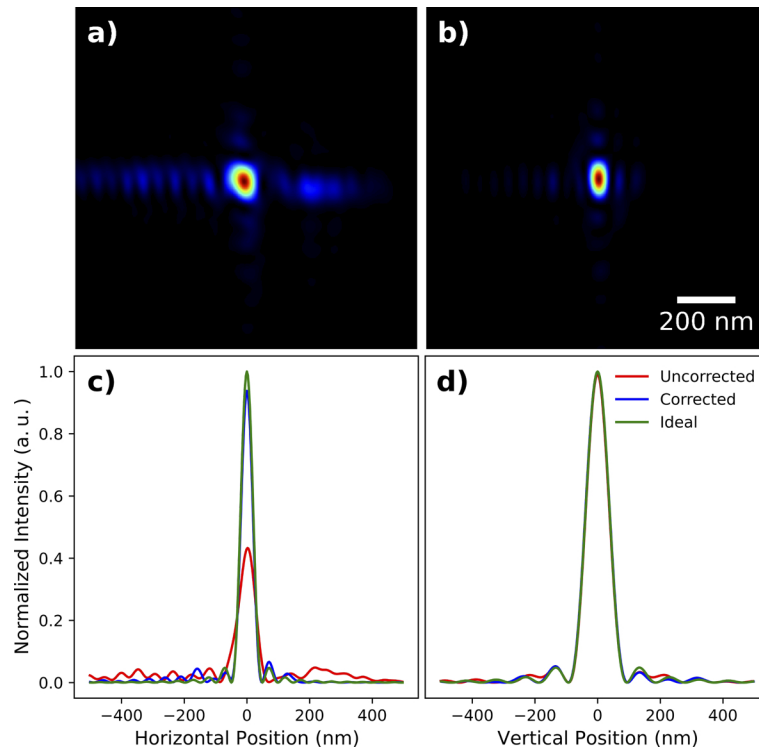


Fig. 4. Intensity profiles at the focal plane after astigmatic correction. The two-dimensional focal intensity distribution a) before b) and after correction. The uncorrected, corrected and ideal one-dimensional focal intensity profiles for c) the HKB and d) the VKB mirrors found using ptychography.

resolution but instead improve the contrast of the resolvable sample features, the most benefit will be observed from samples with spatial features close to the size of the diffraction limit.

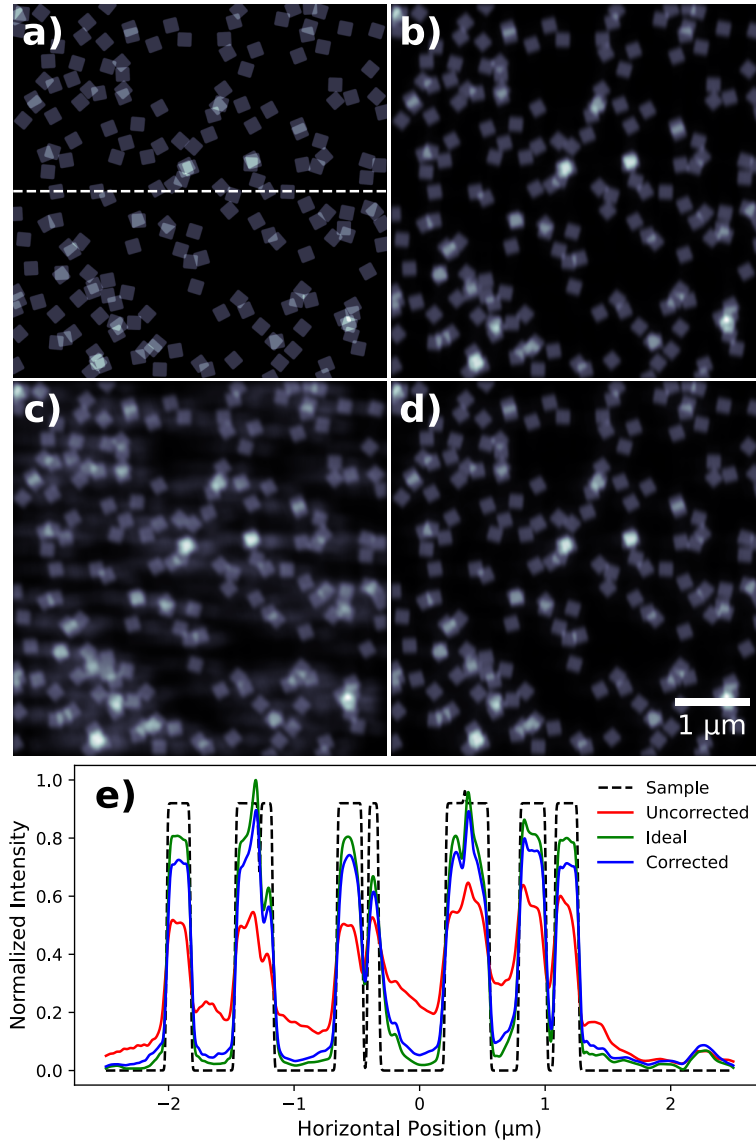


Fig. 5. Simulated scanning X-ray transmission experiment of Au nanocubes using the coherent ptychographic reconstructed probe. The images are transmission intensities corresponding to a) the original sample, b) the ideal probe, c) without corrective optics and d) with corrective optics. e) A line profile indicated by the dashed white line in a).

6. Conclusion

The effects have been presented and studied of using adaptable refractive optics to correct simultaneously the aberrated VKB and HKB focusing mirrors. The results demonstrate that small two-dimensional wavefront errors can be successfully decomposed into horizontal and vertical components, only requiring independent corrective optics for each. Wavefront errors were reduced by a factor of 4 for the HKB and a factor of 1.8 for the VKB, allowing diffraction limited performance of the overall mirror system. Given the VKB mirror was diffraction limited prior to correction and the peak intensity gained is very small, the inclusion of any corrective optics is only likely to reduce the actual peak intensity due to absorption, therefore adaptable refractive structures are most suited for optics with large wavefront errors. The ptychographic technique provided spatial resolution superior to other at-wavelength metrology techniques and was able to model the coherent probe without the need to superimpose the wavefront error on ideal simulated optics, as is traditionally done. Although the coherent fraction of the beam is small, the results demonstrate we are still able to access the performance of the optic and benefits of correction as it would be with a completely coherent source. To illustrate the benefit of such corrective optics we simulated a typical scanning transmission X-ray microscopy experiment of gold nanocubes with a visible gain in contrast and resolution when the correctors were used. As X-ray sources at synchrotrons become ever smaller and produce more coherent flux, the use of multilayer mirrors and higher numerical aperture optics will place greater significance on the fabrication errors. Adaptable refractive correctors have shown promise to offer fast, dynamic and affordable wavefront correction that can be easily installed on pre-existing beamlines. We expect these results to apply to other types of X-ray focusing optics operating over a large energy range in the hard X-ray regime.

Funding. Horizon 2020 Framework Programme (665593).

Acknowledgments. This work was carried out with the support of the Diamond Light Source. The authors thank Andrew Malandain for technical support during the measurements on the B16 Test beamline. Ptychography reconstruction were carried out using the PtyPy frameworks and the High Performance Cluster computing facilities at the Diamond Light Source. P. Mondal, P. Tiwari, and N. Khantwal are acknowledged for their technical assistance during the X-ray lithography fabrication at the Indus-2 synchrotron facility, and we are grateful to Arndt Last from IMT/KIT for providing the LIGA fabricated gold knife edge used in the at-wavelength measurements.

Disclosures. The authors declare no conflicts of interest.

Data availability. Data underlying the results presented in this paper are available in the Zenodo public repository in Ref. [39].

Supplemental document. See [Supplement 1](#) for supporting content.

References

1. A. Schindler, T. Haensel, A. Nickel, H.-J. Thomas, H. Lammert, and F. Siewert, "Finishing procedure for high-performance synchrotron optics," in *Optical Manufacturing and Testing V*, vol. 5180 H. P. Stahl, ed., International Society for Optics and Photonics (SPIE, 2003), pp. 64–72.
2. H. Mimura, S. Handa, T. Kimura, H. Yumoto, D. Yamakawa, H. Yokoyama, S. Matsuyama, K. Inagaki, K. Yamamura, Y. Sano, K. Tamasaku, Y. Nishino, M. Yabashi, T. Ishikawa, and K. Yamauchi, "Breaking the 10 nm barrier in hard-x-ray focusing," *Nat. Phys.* **6**(2), 122–125 (2010).
3. K. Sawhney, D. Laundy, V. Dhamgaye, and I. Pape, "Compensation of x-ray mirror shape-errors using refractive optics," *Appl. Phys. Lett.* **109**(5), 051904 (2016).
4. F. Seiboth, A. Schropp, M. Scholz, F. Wittwer, C. Rödel, M. Wünsche, T. Ullsperger, S. Nolte, J. Rahomäki, K. Parfeniukas, S. Giakoumidis, U. Vogt, U. Wagner, C. Rau, U. Boesenberg, J. Garrevoet, G. Falkenberg, E. C. Galtier, H. Ja Lee, B. Nagler, and C. G. Schroer, "Perfect x-ray focusing via fitting corrective glasses to aberrated optics," *Nat. Commun.* **8**(1), 14623 (2017).
5. D. Laundy, V. Dhamgaye, T. Moxham, and K. Sawhney, "Adaptable refractive correctors for x-ray optics," *Optica* **6**(12), 1484–1490 (2019).
6. K. Sawhney, H. Wang, J. Sutter, S. Alcock, and S. Berujon, "At-wavelength metrology of x-ray optics at diamond light source," *Synchrotron Radiat. News* **26**(5), 17–22 (2013).
7. S. Berujon, E. Ziegler, R. Cerbino, and L. Peverini, "Two-dimensional x-ray beam phase sensing," *Phys. Rev. Lett.* **108**(15), 158102 (2012).

8. M. Idir, P. Mercere, M. H. Modi, G. Dovillaire, X. Levecq, S. Bucourt, L. Escolano, and P. Sauvageot, "X-ray active mirror coupled with a hartmann wavefront sensor," *Nucl. Instrum. Methods Phys. Res., Sect. A* **616**(2-3), 162–171 (2010). X-Ray Mirror.
9. T. Weitkamp, B. Nöhammer, A. Diaz, C. David, and E. Ziegler, "X-ray wavefront analysis and optics characterization with a grating interferometer," *Appl. Phys. Lett.* **86**(5), 054101 (2005).
10. O. Hignette, A. K. Freund, and E. Chinchio, "Incoherent x-ray mirror surface metrology," in *Materials, Manufacturing, and Measurement for Synchrotron Radiation Mirrors*, vol. 3152 P. Z. Takacs and T. W. Tonnessen, eds., International Society for Optics and Photonics (SPIE, 1997), pp. 188–199.
11. P. Thibault, M. Dierolf, A. Menzel, O. Bunk, C. David, and F. Pfeiffer, "High-resolution scanning x-ray diffraction microscopy," *Science* **321**(5887), 379–382 (2008).
12. J. M. Rodenburg, A. C. Hurst, A. G. Cullis, B. R. Dobson, F. Pfeiffer, O. Bunk, C. David, K. Jefimovs, and I. Johnson, "Hard-x-ray lensless imaging of extended objects," *Phys. Rev. Lett.* **98**(3), 034801 (2007).
13. C. M. Kewish, P. Thibault, M. Dierolf, O. Bunk, A. Menzel, J. Vila-Comamala, K. Jefimovs, and F. Pfeiffer, "Ptychographic characterization of the wavefield in the focus of reflective hard x-ray optics," *Ultramicroscopy* **110**(4), 325–329 (2010).
14. A. Schropp, P. Boye, J. M. Feldkamp, R. Hoppe, J. Patommel, D. Samberg, S. Stephan, K. Giewekemeyer, R. N. Wilke, T. Salditt, J. Gulden, A. P. Mancuso, I. A. Vartanyants, E. Weckert, S. Schöder, M. Burghammer, and C. G. Schroer, "Hard x-ray nanobeam characterization by coherent diffraction microscopy," *Appl. Phys. Lett.* **96**(9), 091102 (2010).
15. S. Hönig, R. Hoppe, J. Patommel, A. Schropp, S. Stephan, S. Schöder, M. Burghammer, and C. G. Schroer, "Full optical characterization of coherent x-ray nanobeams by ptychographic imaging," *Opt. Express* **19**(17), 16324–16329 (2011).
16. M. Osterhoff, A.-L. Robisch, J. Soltau, M. Eckermann, S. Kalbfleisch, D. Carbone, U. Johansson, and T. Salditt, "Focus characterization of the NanoMAX Kirkpatrick–Baez mirror system," *J. Synchrotron Radiat.* **26**(4), 1173–1180 (2019).
17. A. Björling, S. Kalbfleisch, M. Kahnt, S. Sala, K. Parfeniukas, U. Vogt, D. Carbone, and U. Johansson, "Ptychographic characterization of a coherent nanofocused x-ray beam," *Opt. Express* **28**(4), 5069–5076 (2020).
18. F. Seiboth, M. Kahnt, M. Scholz, M. Seyrich, F. Wittwer, J. Garrevoet, G. Falkenberg, A. Schropp, and C. G. Schroer, "Quantitative characterization of aberrations in x-ray optics," in *Advances in X-Ray/EUV Optics and Components XI*, vol. 9963 A. M. Khounsary, S. Goto, and C. Morawe, eds., International Society for Optics and Photonics (SPIE, 2016), pp. 88–95.
19. H. Chang, P. Enfedaque, Y. Lou, and S. Marchesini, "Partially coherent ptychography by gradient decomposition of the probe," *Acta Crystallogr., Sect. A: Found. Adv.* **74**(3), 157–169 (2018).
20. T. E. J. Moxham, D. Laundy, V. Dhamgay, O. J. L. Fox, K. Sawhney, and A. M. Korsunsky, "Aberration characterization of x-ray optics using multi-modal ptychography and a partially coherent source," *Appl. Phys. Lett.* **118**(10), 104104 (2021).
21. B. Enders, "Development and application of decoherence models in ptychographic diffraction imaging," Ph.D. thesis, Technical University Munich (2016).
22. T. E. J. Moxham, A. Parsons, T. Zhou, L. Alianelli, H. Wang, D. Laundy, V. Dhamgay, O. J. L. Fox, K. Sawhney, and A. M. Korsunsky, "Hard X-ray ptychography for optics characterization using a partially coherent synchrotron source," *J. Synchrotron Radiat.* **27**(6), 1688–1695 (2020).
23. A. Macrander, M. Wojcik, J. Maser, N. Bouet, and R. Conley, "Focus of a multilayer Laue lens with an aperture of 102 microns determined by ptychography at beamline 1-BM at the Advanced Photon Source," in *X-Ray Nanoimaging: Instruments and Methods III*, vol. 10389 B. Lai and A. Somogyi, eds., International Society for Optics and Photonics (SPIE, 2017), pp. 1–6.
24. J. C. da Silva, A. Pacureanu, Y. Yang, S. Bohic, C. Morawe, R. Barrett, and P. Cloetens, "Efficient concentration of high-energy x-rays for diffraction-limited imaging resolution," *Optica* **4**(5), 492–495 (2017).
25. D. Laundy, S. G. Alcock, L. Alianelli, J. P. Sutter, K. J. S. Sawhney, and O. Chubar, "Partial coherence and imperfect optics at a synchrotron radiation source modeled by wavefront propagation," in *Advances in Computational Methods for X-Ray Optics III*, vol. 9209 M. S. del Rio and O. Chubar, eds., International Society for Optics and Photonics (SPIE, 2014), pp. 1–7.
26. C. Morawe, P. Pecci, J. C. Peffen, and E. Ziegler, "Design and performance of graded multilayers as focusing elements for x-ray optics," *Rev. Sci. Instrum.* **70**(8), 3227–3232 (1999).
27. M. Born, E. Wolf, and A. B. Bhatia, *Principles of optics* (Cambridge University Press, Cambridge, 2019), seventh edition.; seventh (expanded) anniversary edition, 60th anniversary edition. ed.
28. E. Becker, W. Ehrfeld, P. Hagmann, A. Maner, and D. Münchmeyer, "Fabrication of microstructures with high aspect ratios and great structural heights by synchrotron radiation lithography, galvanofarming, and plastic moulding (liga process)," *Microelectron. Eng.* **4**(1), 35–56 (1986).
29. V. P. Dhamgay, G. S. Lodha, B. Gowri Sankar, and C. Kant, "Beamline BL-07 at Indus-2: a facility for microfabrication research," *J. Synchrotron Radiat.* **21**(1), 259–263 (2014).
30. K. J. S. Sawhney, I. P. Dolbnya, M. K. Tiwari, L. Alianelli, S. M. Scott, G. M. Preece, U. K. Pedersen, and R. D. Walton, "A test beamline on diamond light source," *AIP Conf. Proc.* **1234**(1), 387–390 (2010).

31. M. Idir, M. Rakitin, B. Gao, J. Xue, L. Huang, and O. Chubar, "Alignment of KB mirrors with at-wavelength metrology tool simulated using SRW," in *Advances in Computational Methods for X-Ray Optics IV*, vol. 10388 O. Chubar and K. Sawhney, eds., International Society for Optics and Photonics (SPIE, 2017), pp. 209–215.
32. T. B. Edo, D. J. Batey, A. M. Maiden, C. Rau, U. Wagner, Z. D. Pešić, T. A. Waigh, and J. M. Rodenburg, "Sampling in x-ray ptychography," *Phys. Rev. A* **87**(5), 053850 (2013).
33. J. C. da Silva and A. Menzel, "Elementary signals in ptychography," *Opt. Express* **23**(26), 33812–33821 (2015).
34. B. Enders and P. Thibault, "A computational framework for ptychographic reconstructions," *Proc. R. Soc. A* **472**(2196), 20160640 (2016).
35. P. Thibault, M. Dierolf, O. Bunk, A. Menzel, and F. Pfeiffer, "Probe retrieval in ptychographic coherent diffractive imaging," *Ultramicroscopy* **109**(4), 338–343 (2009).
36. P. Thibault and A. Menzel, "Reconstructing state mixtures from diffraction measurements," *Nature* **494**(7435), 68–71 (2013).
37. A. Maiden, D. Johnson, and P. Li, "Further improvements to the ptychographical iterative engine," *Optica* **4**(7), 736–745 (2017).
38. V. N. Mahajan, "Orthonormal aberration polynomials for anamorphic optical imaging systems with rectangular pupils," *Appl. Opt.* **49**(36), 6924–6929 (2010).
39. T. E. J. Moxham, V. Dhamgaye, D. Laundry, O. J. Fox, H. Khosroabadi, K. Sawhney, and A. M. Korsunsky, "Dataset: Two-dimensional wavefront characterization of adaptable corrective optics and Kirkpatrick–Baez mirror system using ptychography," (2022).